Check for updates

View Article Online
View Journal

Energy & Environmental Science

Accepted Manuscript

This article can be cited before page numbers have been issued, to do this please use: M. Melchionna, V. Bracamonte, A. Giuliani, L. Nasi, T. Montini, C. Tavagnacco, M. Bonchio, P. Fornasiero and M. Prato, *Energy Environ. Sci.*, 2018, DOI: 10.1039/C7EE03361C.

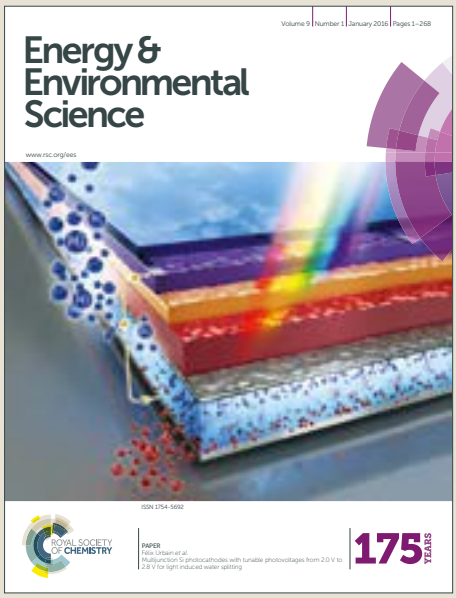

This is an Accepted Manuscript, which has been through the Royal Society of Chemistry peer review process and has been accepted for publication.

Accepted Manuscripts are published online shortly after acceptance, before technical editing, formatting and proof reading. Using this free service, authors can make their results available to the community, in citable form, before we publish the edited article. We will replace this Accepted Manuscript with the edited and formatted Advance Article as soon as it is available.

You can find more information about Accepted Manuscripts in the author guidelines.

Please note that technical editing may introduce minor changes to the text and/or graphics, which may alter content. The journal's standard Terms & Conditions and the ethical guidelines, outlined in our author and reviewer resource centre, still apply. In no event shall the Royal Society of Chemistry be held responsible for any errors or omissions in this Accepted Manuscript or any consequences arising from the use of any information it contains.

ROYAL SOCIETY OF CHEMISTRY

rsc.li/ees

View Article Online
DOI: 10.1039/C7EE03361C

Journal Name

ARTICLE

Pd@TiO_2/Carbon Nanohorns electrocatalysts: Reversible CO_2 hydrogenation to formic acid

Received 00th January 20xx,
Accepted 00th January 20xx

DOI: 10.1039/x0xx00000x

www.rsc.org/

M. Melchionna,[a] M. V. Bracamonte,[a] A. Giuliani,[a] L. Nasi,[b] T. Montini,[a,d] C. Tavagnacco,[a] M. Bonchio,[*,c] P. Fornasiero[*,a,d] and M. Prato[*,a,e]

Direct conversion of carbon dioxide to formic acid at thermodynamic equilibrium is a privilege of enzymatic catalysis, hardly replicated by synthetic analogs, but of high priority for carbon-neutral energy schemes. The bio-mimetic potential of totally inorganic Pd@TiO_2 nanoparticles is envisioned herein in combination with Single Walled Carbon NanoHorns (SWCNHs). The high surface nano-carbon entanglement templates a wide distribution of "hard-soft" bimetallic sites where the small Pd nanoparticles (1.5 nm) are shielded within the TiO_2 phase (Pd@TiO_2), while being electrically wired to the electrode by the nanocarbon support. This hybrid electrocatalyst activates CO_2 reduction to formic acid at near zero overpotential in aqueous phase (onset potential at E < -0.05 V vs RHE, pH = 7.4), while being able to evolve hydrogen via sequential formic acid dehydrogenation. The net result hints at a unique CO_2 "circular catalysis" where formic acid versus H_2 selectivity is adressable by flow-reactor technology.

Introduction

Electrocatalytic hydrogenation of CO_2 to formic acid (HCO_2H) and/or to its conjugate base, formate (HCO_2^-), is of central importance for carbon-neutral energy schemes, where CO_2 is used as reversible storage/release vector for H_2-based technologies [1]. CO_2 reduction is used by Nature as a key strategy to store energy into chemical bonds. However, its artificial replica under abiotic conditions is highly inefficient due to severe thermodynamic and kinetic hurdles related to CO_2 capturing and activation [2].

A new paradigm has been recently introduced by the direct use of purified Formate Dehydrogenase (FDH) enzymes as electrocatalysts, which provides a definite landmark for the CO_2/formate interconversion with fast rates in water at neutral pH [2-4]. FDH-based electrocatalysis is conceptually unique vis-à-vis the near-equilibrium working potential [(E CO_2/HCO_2^-) = -0.02 V at pH 7 vs RHE] and its product specificity [3-5]. However, this approach is plagued by protein purification and stability issues, together with formidable scaling-up problems, which hamper any viable exploitation. Therefore, the invention of synthetic catalysts and functional electrodes mimicking the enzymatic performance with robust chemical architectures remains a priority for selective CO_2 processing [1, 3]. Up to now, while several bio-inspired molecular catalysts and nano-materials have been successfully developed for the electrocatalytic reduction of CO_2 to CO, the two-electron hydrogenation to formate is still achieved with a too high overpotential, poor selectivity and limited appeal [2]. Recent case-studies highlight that a functional synergy of the active metal-site with its proximal environment provides a key strategy for: (i) capturing CO_2 by favorable absorption/activation equilibria; (ii) low-energy proton coupled electron transfer mechanisms (PCET); (iii) the stabilization of selective hydride intermediates enabling direct hydrogenation of CO_2[3]. In this notion, the "ideal" catalyst should be effective for both the direct CO_2-to-HCO_2H conversion, and the back-dehydrogenation reaction, that eventually liberates H_2 and CO_2 from HCO_2H decomposition. According to this scheme, the CO_2/HCO_2H interconversion through reversible and/or sequential catalytic steps is of central importance as it expands the scope of formic acid synthesis, from a pure commodity "niche" chemical (ca. 800 kton/year) to a liquid source of H_2 storage (4.3 wt%) with a carbon-neutral net balance[6-8].

Continuous H_2 production is currently pursued through direct proton/water electrocatalytic reduction. However and despite some recent encouraging systems using earth-abundant, non-noble metals electrocatalysts, such as cobalt[9, 10], molybdenum[11, 12], and iron[13], costly Pt-based cathodes are still the preferred choice on account of their low overpotential, wide pH range applicability and high turnover performance [14-16]. Therefore, the alternative CO_2 →

[a] Department of Chemical and Pharmaceutical Sciences, INSTM. University of Trieste, Via L. Giorgieri 1, 34127 Trieste, Italy.
[b] CNR-IMEM Institute, Parco area delle Scienze 37/A, 43124 Parma, Italy.
[c] ITM-CNR and Department of Chemical Sciences, University of Padova, Via F. Marzolo 1, 35131 Padova, Italy
[d] ICCOM-CNR, University of Trieste, Via L. Giorgieri 1, 34127 Trieste, Italy.
[e] Carbon Nanobiotechnology Laboratory, CIC biomaGUNE, Paseo de Miramón 182, 20009 Donostia-San Sebastian (Spain).
Basque Fdn Sci, Ikerbasque, Bilbao 48013 (Spain)

† Footnotes relating to the title and/or authors should appear here.
Electronic Supplementary Information (ESI) available: [details of any supplementary information available should be included here]. See DOI: 10.1039/x0xx00000x

Published on 06 April 2018. Downloaded by Fudan University on 06/04/2018 19:06:53.

Energy & Environmental Science Accepted Manuscript

Please do not adjust margins

View Article Online
DOI: 10.1039/C7EE03361C

Published on 06 April 2018. Downloaded by Fudan University on 06/04/2018 19:06:53.

$HCO_2H \rightarrow H_2 + CO_2$ cycle, where CO_2 mediates water reduction/hydride transfer mechanisms at the gas-liquid interface, provides an appealing electrocatalytic route for a CO_2-circular hydrogen economy.

Modified electrodes able to favourably and selectively reduce CO_2 based on the use of noble metals have been massively investigated, with platinum being surely the most employed metal even in recent reports [17-19]. Pd is a possible intriguing alternative due to the lower cost as compared to Pt or Au, as well as its recently reported low toxicity [20], which alleviates scaling-up issues. Pd-containing electrocatalysts have been successfully tuned to target CO_2 electro-hydrogenation in combination with carbon-rich supports [21], conductive polymers [22] or Pt-heterojunctions [23]. In particular, we have recently shown that Pd nanoparticles (Pd-NPs) on single wall carbon nanotubes trigger the direct electrocatalytic water reduction at neutral pH and with low applied potentials (50 mV) [24]. Pd-based nanocatalysts have also been shown recently to perform dehydrogenation of formic acid at ambient temperature[25]. Following these concepts, we report herein the integration of Pd nanoparticles (Pd-NPs) on oxidized Single Walled Carbon NanoHorns (ox-SWCNHs) and stabilized by a TiO_2 outer-shell, by taking inspiration from previous studies by some of us on embedded Pd nanoparticles into oxide matrices and hierarchical catalysts[26-29]. The resulting Pd@TiO_2/ox-SWCNHs heterostructures feature an unprecedented triple-junction electrocatalytic interface that is effective for a cascade transformation involving the CO_2-to-HCO_2H reduction and the HCO_2H-to-H_2 decomposition, thus using CO_2 as an organo-catalytic mediator (Scheme 1). The resulting electrocatalyst enables the selective CO_2 reduction at mild potential (~ -0.2 V vs RHE) as the dominant pathway, overriding the competitive reduction of water to hydrogen (HER mechanism, at ~ -0.4 V vs RHE). Noteworthy H_2 evolution is observed over time, as a product of the catalytic decomposition of formic acid accumulating in the system. Indeed, under CO_2-free conditions, no H_2 is observed, underpinning the key role of CO_2 as intermediate. Our results point to the electrocatalytic formation of "Pd-H" intermediates at the crossroad of concurrent hydrogenation/de-hydrogenation pathways, involving the CO_2/HCO_2H couple. The final outcome is a continuous H_2 evolution at lower overpotential (200 mV gain), in the presence of a steady–state formic acid concentration, implying a circular CO_2 consumption/release process. Taking advantage of the exceptionally high faradaic efficiency of the HCO_2H production (up to ~95% in the initial 5 minutes then reaching a 40% yield after 1 h), a kinetic control of the reaction profile under flow regime is envisaged herein as a tool to switch the product selectivity favouring the commodity chemical. Indeed, when the HCO_2H product is extracted from the electrolysis phase at selected chronoamperometry – time intervals, H_2 evolution is stopped while the formate selectivity is restored and this behaviour is confirmed in multiple on/off experiments.

Results and discussion

Synthesis and characterization of the electrocatalytic Pd@TiO_2/ox-SWCNHs heterostructures:

The synthetic design of the organic-inorganic nano-material has been planned with the twofold aim of: (i) exploiting the high surface area and morphology of the nanohorn scaffold (SWCNH) as template; (ii) providing the the "soft" Pd sites within a "hard" TiO_2 metal-oxide environment. This latter aspect is instrumental to control CO_2/H_2O binding equilibria at bimetallic sites[30], while favoring Pd-hydride phases, and shielding the ultra-small Pd-NPs against irreversible agglomeration and poisoning (Scheme 1) [31, 32]. Moreover, the SWCNHs connectivity guarantees the electrical wiring of the Pd-active sites, as a result of their unique conical geometry with protruding nano-tips, that work as terminal "electron collectors" and boost charge mobility [33, 34]. Such behavior is further implemented by the SWCNHs strong tendency to aggregate into flower-like superstructures, with increased surface area and improved gas adsorption behavior[35]. Gas absorption is expected to modulated the SWCNH conductivity properties[36].

The Pd@TiO_2 precursors are readily obtained following a literature protocol [37] and used for the sol-gel integration of oxidized SWCNHs (ox-SWCNHs). Controlled oxidation of SWCNHs yields an optimal surface distribution of carboxylate (COOH) and/or epoxy-alcoholic functions (C-O-C, C-OH), needed to anchor the sol-gel blend. The oxidation treatment is also instrumental to the opening of reactive nano-windows (i.e. opening of the SWCNHs tips and defects in the polyaromatic framework) [38], that further enhance the material surface area (ox-SWCNHs, BET ~1400 $m^2 g^{-1}$) and its interaction with the sol-gel matrix [39].

Energy & Environmental Science Accepted Manuscript

This journal is © The Royal Society of Chemistry 20xx

Please do not adjust margins

View Article Online
DOI: 10.1039/C7EE03361C

Published on 06 April 2018. Downloaded by Fudan University on 06/04/2018 19:06:53.

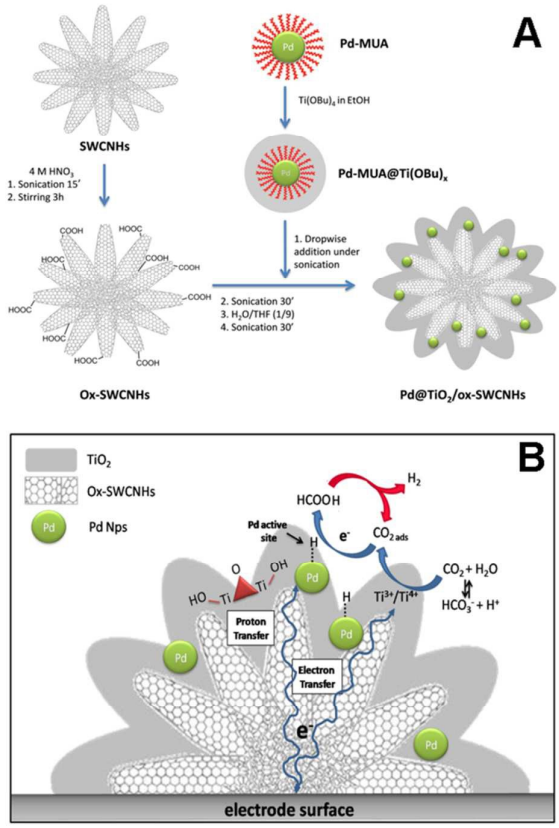

Scheme 1. A) Schematic synthesis of Pd@TiO_2/ox-SWCNHs hetero-structures by sol-gel inclusion of capped Pd-NPs (MUA = mercaptoundecanoic acid) within a TiO_2 shell, upon controlled hydrolysis in the presence of oxidized SWCNHs, and B) scheme of the electrocatalytic hydrogenation mechanism envisaged for the conversion of CO_2 to formic acid (blue arrows) and its decomposition (red arrows) at the Pd@TiO_2/ox-SWCNHs triple functional interface (-0.2 V vs RHE). For convenience we presented a 2D section of the electrocatalytic material.

Thermogravimetric analysis (N_2-TGA) has been used to assess the degree of SWCNH oxidative functionalization, which accounts for an 11 % by weight (Figure S1, supporting information). The target nano-hybrid Pd@TiO_2/ox-SWCNHs is finally obtained after controlled hydrolysis of the Ti alkoxide precursors in a H_2O/THF solvent mixture. As a term of comparison, the Pd-free analogue, TiO_2/ox-SWCNHs, is obtained by a similar sol-gel strategy. O_2-TGA analysis of both hybrid materials indicates that the carbon phase accounts for about 75 wt %, with the remaining 25 wt % being ascribed to the metal-oxide components, in agreement with the synthetic protocol conditions. Analogously, the approximate overall content of Pd is calculated to be about 1.5 wt %. Such value is further confirmed by ICP-AES analysis of the material, which provides an exact loading of 1.45%. The intimate carbon/metal/metal oxide contact of the hybrid material is responsible for the anticipation (by about 50°C) of the onset of combustion temperature as compared to the SWCNH scaffold alone. This effect is caused by the presence of the Pd nanoparticles which can catalyze the combustion of the carbon scaffold.

Direct evidence of the materials morphology is obtained by High Resolution Transmission Electron Microscopy (HRTEM), in combination with High-Angle Annular Dark-Field imaging (HAADF) and the Energy-Dispersive X-ray spectroscopy (EDX) element mapping, collected for the resulting materials at three stages of fabrication complexity, namely: ox-SWCNHs, TiO_2/ox-SWCNHs and Pd@TiO_2/ox-SWCNHs (Figure 1). Inspection of the microscopy images confirms: (i) the supramolecular architecture of the SWCNH secondary aggregates with diameter in the range 50-80 nm (ox-SWCNHs Figure 1A); (ii) adhesion of a thin shell of TiO_2 decorating the SWCNH particles at their outer rim and protruding edges

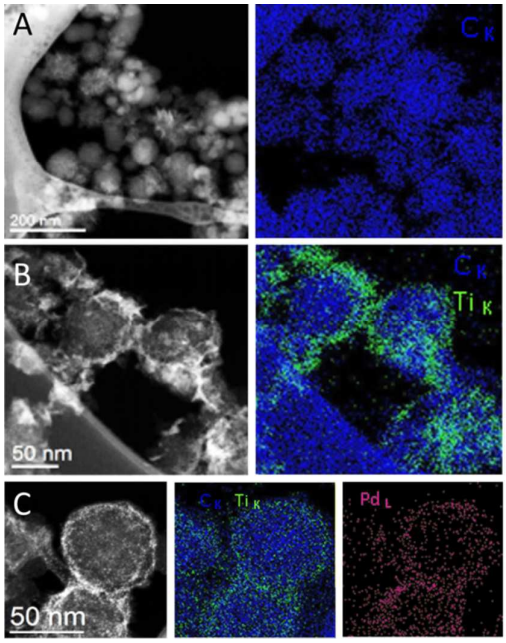

Figure 1. Representative HAADF (black and white) and corresponding EDX maps (colours) of the SWCNH-based hetero-structures: A) ox-SWCNHs, B) TiO_2/ox-SWCNHs, C) Pd@TiO_2/ox-SWCNHs.

(TiO_2/ox-SWCNHs Figure 1B); (iii) the embedding of ultra-small Pd-NPs with average diameter of 1.5 nm and a standard deviation of 0.36 nm (Figure 2), co-localized with the metal-oxide phase, displaying a broad coverage all over the interdigitated SWCNH phase (Pd@TiO_2/ox-SWCNHs Figure 1C). Homogeneous dispersion of the Pd NPs is well visible in the HAADF-STEM as bright spots, from where the particle size distribution was calculated (Figure 2A and S14). Notably, HAADF-STEM inspection of the material after catalysis shows no change of the structure, with the Pd NPs not undergoing any aggregation (Figure S15).

In accordance with the very low thermal treatment of the present materials, Fast Fourier Transform (FFT) and selected area electron diffraction (SAED) analyses did not reveal any crystalline area for TiO_2, which turns out to be amorphous. This may be one of the parameters defining the electrocatalytic properties of the material. Namely, the onset potential for the competing water electrolysis is in our case significantly more negative than that found for the CNT-based analogue material, where the titania layer was crystallized

Energy & Environmental Science Accepted Manuscript

Please do not adjust margins

View Article Online
DOI: 10.1039/C7EE03361C

Published on 06 April 2018. Downloaded by Fudan University on 06/04/2018 19:06:53.

through a thermal annealing [24]. This imparts a wider potential window between the CO_2 reduction and the proton reduction processes, contributing to enhance selectivity and driving the mechanism of HER.

Raman spectra collected for ox-SWCNHs show the typical D and G bands pattern for these nanostructures: the defect-induced D band at ~1330 cm^{-1}, the graphitic G band at ~1580 cm^{-1} and the D second order harmonic 2D band ~2665 cm^{-1} (Figure S2A, black trace). The ratio between the intensities of the D and G bands (I_D/I_G ratio) is a semiquantitative indication of the degree of covalent modification of the conjugate framework. In the oxidized ox-SWCNHs, the I_D/I_G ratio (~1.27) is not significantly affected with respect to the pristine material, as a result of mild oxidation conditions thus indicating a minimal perturbation of the SWCNH properties by surface defects [40]. In agreement with the SAED analysis, no peaks associated to crystalline TiO_2 modes are observed in the Raman spectra of TiO_2/ox-SWCNHs or Pd@TiO_2/ox-SWCNHs (Figure S2A, red and green traces) due to its amorphous phase. Consistently, irradiation with higher Raman laser powers (> 5 mW) induces local crystallization, proved by the appearance of five Raman peaks characteristic of TiO_2 anatase phase at 146 cm^{-1}, 198 cm^{-1}, 395 cm^{-1}, 513 cm^{-1} and 639 cm^{-1} [41] (Figures S2B and S3). FT-IR analysis has been used to address the surface functional groups of the final nano-hybrid Pd@TiO_2/ox-SWCNHs (Figure S4), whereby signature peaks observed at ~800, 1100, 1400, 1600, and 3400 cm^{-1}, are respectively ascribed to the vibration modes of the metal-oxide O-Ti-O groups [24], and of the C–O, C=C and C=O moieties of the carbon phase, while the broad O-H absorption band likely includes the contribution of C-O-H, (CO)O-H and Ti-O-H functions [42]. Therefore, FT-IR evidence points to the presence of a hydrated coordination sphere, settled on the metal-oxide phase, that mitigates the hydrophobicity of the nano-carbon scaffolds, while promoting the proton/hydride transfer reaction at the Pd-active sites under reducing conditions (Scheme 1).

The accessibility of the Pd-NPs has been probed by CO chemisorption experiments on Pd@TiO_2/ox-SWCNHs, performed at 35 °C, which confirm the TiO_2 porous structure (Figure S5), yielding a Pd surface area of about 1.47 m^2 g^{-1} (Figure S6). This value is consistent with the size and the amount of Pd-NPs present in the sample. Furthermore, the specific surface area (BET) of the Pd@TiO_2/ox-SWCNHs hybrid remains significant (BET ~148 m^2 g^{-1}), as shown by N_2 physisorption analysis (Figure S7). Hence, the porosity of the TiO_2 matrix allows accessibility of the embedded Pd nanoparticles.

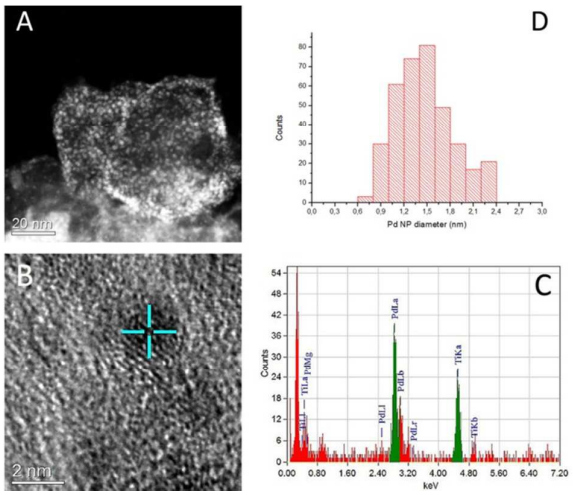

Figure 2. Representative STEM of catalysts Pd@TiO_2/ox-SWCNHs (A), HRTEM showing the size of the Pd nanoparticles (B), EDX spectrum (C) and Pd particle size distribution calculated from STEM images

Electrochemical characterization and bulk electrocatalysis experiments

The electrocatalytic activity of the hierarchical nano-hybrids has been initially evaluated by Cyclic Voltammetry (CV) experiments, performed in phosphate buffer (pH=7.4), with a scan rate of 30 mV s^{-1} under both, N_2- and CO_2-saturated solutions (Figure 3). The control survey obtained under N_2 saturation, for the material precursors and for the final nano-hybrid confirms the inertness of the ox-SWCNHs within the explored potential window (black line in Figure S8), while the redox signatures registered at -0.65 V and -0.35 V vs RHE for TiO_2/ox-SWCNHs can be readily ascribed to Ti^{4+}/Ti^{3+} sites of the metal-oxide shell [43]. Noteworthy, the CV curve registered for Pd@TiO_2/ox-SWCNHs appears to be dominated by the Pd-NPs (green line in Figure S8). These are responsible for two cathodic peaks centered at 0.40 V and -0.25 V vs RHE ascribed to the reversible reduction of PdO formed during the oxidative potential scan at E > 0.65 V vs RHE [44, 45]. Noteworthy, in accordance with previous studies [24], the electrocatalytic HER arising from the water reduction is visible in the CV scan under N_2 as a cathodic wave with onset potential at about -0.4 V vs RHE. Calculation of the electroactive surface area (EASA) for the Pd@TiO_2/ox-SWCNHs modified electrodes is readily accomplished by considering the need of a charge value of 405 μC cm^{-2} for the reduction of the PdO monolayer, which yields an EASA value of (0.22 ± 0.04) cm^2 which corresponds to ~17 m^2 g^{-1} after normalization by the grams of catalyst. For the sake of comparison, we prepared a TiO_2-free reference, Pd/ox-SWCNHs, with a nominal Pd title of 1.5%, via $NaBH_4$ reduction of the K_2PdCl_4 precursor, after adsorption onto the ox-SWCNH. TEM analysis confirms the presence of the Pd-NPs onto the nanocarbon scaffold (Figure S9), while the resulting electrode displays a calculated EASA (0.15 ± 0.02) cm^2, thus providing a key control material. It must be noted that the TiO_2-free material has a broader particle size dispersion (Figure S9) with averagely larger Pd nanoparticles. Nevertheless, a reliable esteem of the effect of the

Energy & Environmental Science Accepted Manuscript

This journal is © The Royal Society of Chemistry 20xx

Please do not adjust margins

View Article Online
DOI: 10.1039/C7EE03361C

Published on 06 April 2018. Downloaded by Fudan University on 06/04/2018 19:06:53.

TiO_2 can be gathered by the observed onset potentials, being associated to the mechanism of catalysis. Moreover, the Pd/ox-SWCNHs serves as reference to evaluate the stability of the catalyst (see later). The CV scans highlight the different response of ox-SWCNHs (A), TiO_2/ox-SWCNHs (B), Pd/ox-SWCNHs (C) and Pd@TiO_2/ox-SWCNHs (D) modified GC electrodes when exposed to a CO_2-saturated solution (pH to 6.5) as compared to N_2 saturation conditions (red vs black lines, Figure 3). While the modest current variation observed for ox-SWCNHs is likely ascribed to a conductivity change of the nano-carbon scaffold under CO_2 saturated conditions (red line, Figure 3A), the redox shift and catalytic current registered for TiO_2/ox-SWCNHs indicates the occurrence of coordination equilibria and CO_2 electrocatalytic reduction at > -0.65 V vs RHE (red line, Figure 3B). When Pd-NPs are integrated into the nano-catalyst formulation, yielding either Pd/ox-SWCNHs or Pd@TiO_2/ox-SWCNHs, a remarkable enhancement of the electrodic response is noted for both catalysts under CO_2 (red line, Figure 3C and 3D). However, a strikingly different behaviour is observed for the final Pd@TiO_2/ox-SWCNHs nano-hybrid, in comparison with all the other combinations (cfr Figures 3A-C with Figure 3D). The catalytic increase of the cathodic current produces two well-defined peaks observed respectively at E_1 = -0.45 V and E_2 = -0.69 V vs RHE. A steep current increase occurs already at E < -0.05 V, leading to a four-fold enhancement of the faradaic density current at -0.45 V, when compared to the TiO_2/ox-SWCNHs/GCE response, and to a clear shift of the reduction onset (ca. 55 mV), with respect to Pd/ox-SWCNHs.

These observations point to a synergy of the ternary Pd@TiO_2/ox-SWCNHs hybrid catalyst in the electrocatalytic reduction of CO_2 at low overpotential regime, showing that all three components are necessary to access a superior catalytic behavior (Figure 3D). The selectivity of the electrocatalytic reduction by Pd@TiO_2/ox-SWCNHs has been addressed under bulk-electrolysis conditions at constant applied potential (-0.2 V vs RHE), using a standard three-electrode cell, integrating a Ag/AgCl (3 M KCl) reference electrode and a Pt counter electrode, with a Pd@TiO_2/ox-SWCNHs modified Toray carbon working electrode.

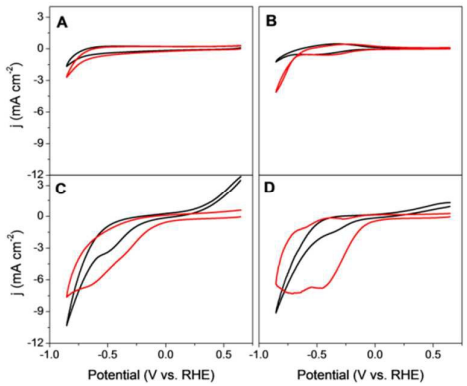

Figure 3. CVs at GCE modified with ox-SWCNHs (A), TiO_2/ox-SWCNHs (B), Pd/ox-SWCNHs (C) and Pd@TiO_2/ox-SWCNHs (D) in N_2 (–) and CO_2 (–) saturated 0.1 M phosphate buffer solution pH 7.4. Scan rate: 0.05 V·s^{-1}.

The product faradaic efficiency (% FE, see equations in the Experimental Section) was determined upon quantitative analysis of the electrolysis solution and head space, performed by Ionic Liquid and Gas Chromatography (ILC, GC). At the applied potential as low as -0.2 V vs RHE (0.1 M phosphate buffer (pH=7.4), formic acid selectivity peaks within the first 5 minute of electrolysis, yielding a maximum of 75% FE, while H_2 accounts for the remaining 25%. At longer run times, H_2 evolution dominates with > 95% FE after 1 hour electrolysis. Isotope labelling experiments (using of $^{13}CO_2$) confirm that formic acid accumulating during electrolysis (ca. $1.6 \cdot 10^{-6}$ mol, mass activity: 9 mA mg_{Pd}^{-1}) is produced from CO_2 as detected by mass spectrometry (Figure S10) and NMR (Figure S11). To address the origin of H_2 evolution, control experiments were performed under inert Ar atmosphere (Figure 4, black line) showing that: (i) in the absence of CO_2, the current density remains low (j_{tot} ~ -0.50 mA cm^{-2}) with no H_2 evolution; (ii) formic acid addition (0.23 M) produces a sharp recovery of a negative current density with simultaneous production of CO_2 and H_2 (Fig 5a); (iii) a similar behaviour is also observed in the absence of PBS buffer, using $NaClO_4$ as supporting electrolyte (pH after CO_2 saturation < 4, see Figure 4, red line).

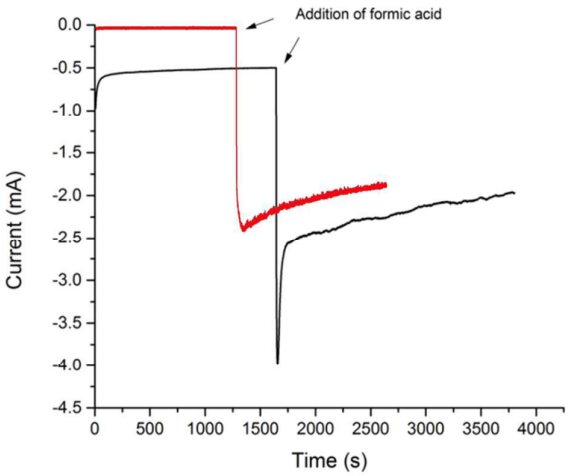

Figure 4. Chronoamperometry of GC electrode modified with Pd@TiO_2/ox-SWCNHs at -0.2 V (vs RHE) in PBS pH 6.5 under Ar flow with addition of formic acid (black line) and Chronoamperometry of Pd@TiO_2/ox-SWCNHs at -0.13 V (vs RHE) in $NaClO_4$ pH 3.6 under Ar flow with addition of formic acid (red line). Quantity of formic acid added: 70 µL, final concentration of formic acid 0.23 M.

These observations point to a step-wise mechanism where HCO_2H is initially formed from CO_2 and then decomposed by Pd@TiO_2/ox-SWCNHs, thus reaching a steady state concentration under electrocatalytic regime. Pd nanoparticles have been reported to decompose formic acid at neutral pHs and in the presence of basic sites[46]. In the present case, H_2 evolution is ascribed to decomposition of the electrocatalytically generated HCO_2H, thus implying a mechanism based on CO_2 cycling, promoted at Pd@TiO_2/ox-SWCNHs and favoured with respect to the direct water reduction. In order to reduce HCO_2H decomposition, bulk

Energy & Environmental Science Accepted Manuscript

Please do not adjust margins

View Article Online
DOI: 10.1039/C7EE03361C

Published on 06 April 2018. Downloaded by Fudan University on 06/04/2018 19:06:53.

electrolysis was performed in unbuffered solution (pH=3.6, CO_2 atmosphere, 0.5 M $NaClO_4$) at -0.13 V (vs RHE). Under these conditions, HCO_2H is produced with quantitative yield (FE> 99%) in the first 5 minutes of electrolysis, and it levels off to a 40% FE after 1 h, upon H_2 evolution (60% FE) observed as a product of formic acid decomposition (Figure 5). Rates of formation of HCOOH and H_2 show that there is an induction time in the production of H_2 due to the initial build-up of formic acid in solution (Figure 5).

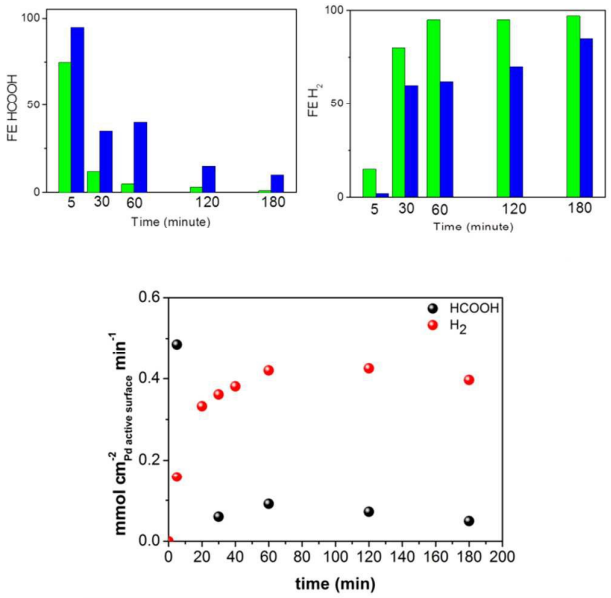

Figure 5. Top: Faradaic Efficiency in formic acid (left) an in hydrogen (right) over time at different times of the chronoamperometric experiments in PBS (green bars) and $NaClO_4$ (blue bars); Bottom: Rates of formation of H_2 and HCOOH by Pd@TiO_2/ox-SWCNHs in NaClO4 electrolyte over three hour long electrocatalytic experiments.

Long-term performance and electrocatalyst stability

Under bulk electrolysis conditions (-0.20 V, 0.10 M phosphate buffer, pH 7.4) the total geometric current density (j_{tot}) settles at a value of ~ -2.00 mA cm^{-2} and maintains a very stable profile, with a negligible, < 5%, decrease over 48 h of electrolysis (Figure S12). The Pd@TiO_2/ox-SWCNHs stability turned out to be excellent even at higher potentials (-0.30 V and -0.35 V, Figure 6A), although increasing the overpotential resulted in a decrease of the FE in formic acid. The improved stability supplied by the titania layer was confirmed by comparing the catalytic stability of the Pd@TiO_2/ox-SWCNHs with that of Pd/ox-SWCNHs under the same catalytic conditions. In contrast with Pd@TiO_2/ox-SWCNHs, the TiO_2-free catalyst undergoes a fast deactivation at -0.2 V, with current density decreasing of about 50 % already after 3 hours (Figure 6B). This fact was already observed in a previous study by Kanan *et al*. and ascribed to aggregation of the Pd NPS over electrolysis time with consequent decrease of the EASA [21].

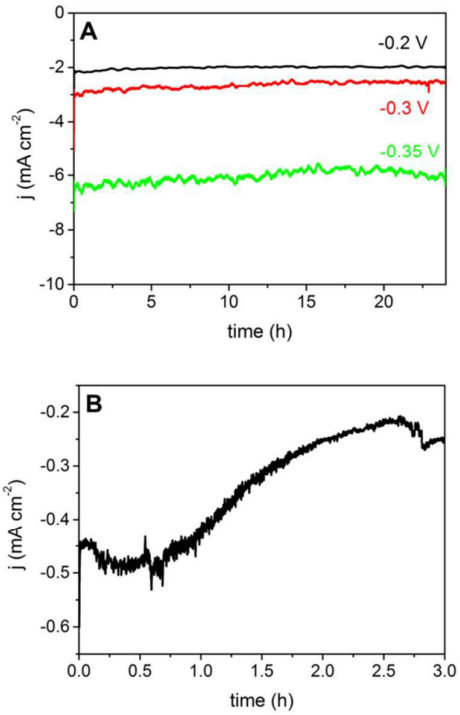

Figure 6. Current-time profile for Pd@TiO_2/ox-SWCNHs maintained at -0.2 V (black line), -0.30 V (red line) and -0.35 V (green line) (vs. RHE). Supporting electrolyte: 0.10 M phosphate buffer solution pH 7.4. The Toray carbon electrode modified by drop casting using 200 µL 3.0 mg mL^{-1} of A) Pd@TiO_2/ox-SWCNHs and B) Pd/ox-SWCNHs. Fixed potential in B is of -0.20 V.

Indeed, TEM analysis of the recovered Pd/ox-SWCNHs catalyst shows a significant NP aggregation after 3 hours of electrolysis, and particle leaching (Figure S13). Hence, the remarkable current stability proves the effectiveness of the TiO_2 phase in preventing the Pd-NPs agglomeration and leaching. In addition to Pd sintering, the drop in current was also related by Kanan to a poisoning of the Pd NPs over time due to concomitant formation of CO, which can coordinate to the metal and inhibit the active sites. In the present case, the selectivity of the CO_2 reduction step was extremely high, with no CO detected through continuous gas chromatography sampling of the cell head-space at 20 minutes intervals, which also ruled out the presence of any other carbon-derived gases such as methane and ethylene. A control experiment was performed by adding CO (0.5%) to the gas mixture, confirming the poisoning effect on Pd@TiO_2/ox-SWCNHs, with a ca. 20% of current loss.

The electrocatalyst selectivity and current performance is maintained upon recycling of the functional electrode in a sequence of three chronoamperometric experiments, switched off after one hour electrolysis (see Figure S16). In these experiments the electrolysis solution, where formic acid accumulates, is replaced at an early stage of the process, so to guarantee a continuous peak formation of HCO_2H by the Pd@TiO_2/ox-SWCNHs electrocatalyst, slowing down its decomposition. This strategy can be efficiently

Energy & Environmental Science Accepted Manuscript

This journal is © The Royal Society of Chemistry 20xx

Please do not adjust margins

View Article Online
DOI: 10.1039/C7EE03361C

Published on 06 April 2018. Downloaded by Fudan University on 06/04/2018 19:06:53.

implemented under flow-regime, by taking advantage of the high FE (> 99%) achieved for HCO_2H at low contact time.

Notably, the catalyst intrinsic activity is achieved with low Pd loadings (nominal Pd loading 1.5% wt.), which highlights the unique role of the hierarchical nano-interfaces to boost CO_2 activation. The turnover frequency (TOF) for the optimized H_2 evolution can be calculated from chronoamperometric experiments (see calculation details in SI) and turns out to be ~26500 h^{-1} at -0.2 V in PBS, by far exceeding the performance of state-of-the-art formic acid dehydrogenation catalysts, namely Pd-NPs on carbon nanospheres (~7300 h^{-1}) [47].

In analogy with the recent work by Kanan and coworkers, the electrocatalytic mechanism probably involves the generation of Pd-H active sites responsible for the selective CO_2 reduction to formic acid (Scheme 1) [21]. This proposal is supported by Tafel analysis (Figure 7) evaluating the dependence of the electrocatalytic rate (log J) on the applied potential. The resulting Tafel plot is characterized by two different regimes, with a calculated slope of (149 ± 6) mV dec^{-1} at low overpotentials (E < -0.2 V), followed by a significant leveling off to a slope of (400 ± 16) mV dec^{-1}. These values are in perfect agreement with the electrocatalytic response expected for Pd NPs as the competent hydrogenation sites [21]. In particular the Tafel slope of (149 ± 6) mV dec^{-1}, which is consistent with a Pd-mediated hydride transfer mechanism, turns out to be the dominating regime also at higher J values, up to -0.2 V, with no mass transfer limitations.

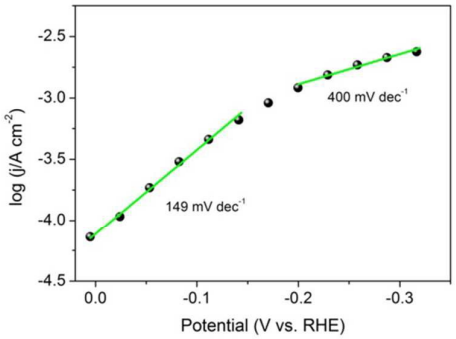

Figure 7. Tafel (Potential vs log j) plot in CO_2-saturated 0.10 M phosphate buffer solution pH 7.4. The current density (j) values were obtained from a linear sweep voltammetry experiment performed at 5 mV s^{-1}. The Tafel plot exhibited an slope of (149 ± 6) mV dec^{-1} from 0.005 V to -0.15 V and 400 mV dec^{-1} at larger overpotentials. The reported slopes are an average of 3 different measurements.

Experimental Section

Materials

Titanium butoxide (97 %, $Ti(OBu)_4$), Nafion® 117 solution, mercapto-undecanoic acid (MUA) and tetrahydrofuran (THF) were purchased from Sigma-Aldrich. Single wall carbon nanohorns were from Carbonium SRL, France. Absolute ethanol, Methanol anhydrous ultra-pure grade and nitric acid (65 %) were purchased from VWR Chemicals. Sodium phosphate dibasic anhydrous and sodium phosphate monobasic were purchased from Carlo Erba. $^{13}CO2$ was purchased from Sigma-Aldrich and it contains 99% of ^{13}C.

Synthesis of oxidized SWCNHs

Pristine SWCNHs were dissolved in a 4 M nitric acid solution in order to obtain a suspension of 1 mg mL^{-1}. The suspensions were sonicated for 15 minutes to dissolve the present bundles and then stirred for three hours. This optimized time is suitable to obtain the optimal degree of oxygenic groups and the lowest damage on the honeycomb structure surface [48, 49]. The solid was then filtered and washed with distilled water until neutral pH of the washing water (ox-SWCNHs).

Synthesis of the electrocatalysts

Electrocatalysts were synthesized by an adapted method previously described by Cargnello et al. [50]. Briefly, the appropriate amount of MUA–protected Pd nanoparticle (Pd-MUA) was dissolved in the needed amount of Titanium butoxide $Ti(OBu)_4$, in order to get the desired ratio components. The solution of $Pd@TiO_2$ precursor was added dropwise to ox-SWCNHs suspension (0.25mg mL^{-1} in EtOH) under continuous sonication. The resulting suspension of "$Pd@Ti(OBu)_4$/ox-SWCNHs" was vigorously sonicated for 30 minutes. Finally, a mixture of H_2O (1.5 mL) and THF (13.5 mL) was added to ensure the complete hydrolysis of the Ti alkoxide. The mixture was sonicated for further 30 min and then the product was filtered through a 0.45 µm PTFE filter, washed with MeOH/H_2O 2:1 v/v and finally with MeOH. The final materials were dried at 80 °C overnight prior to being used ($Pd@TiO_2$/ox-SWCNHs). A similar approach was adopted in the absence of Pd-MUA in order to obtain the corresponding Pd-free catalyst (TiO_2/ox-SWCNHs).

For the synthesis of Pd/ox-SWCNHs, the ox-SWCNHs were sonicated in EtOH, and the appropriate amount of K_2PdCl_4 was added and the mixture sonicated for 30 minutes. An aqueous solution of $NaBH_4$ was added and the mixture sonicated for another 15 minutes. It was then filtered through a 0.45 µm PTFE filter and the solid washed with water, followed by EtOH washing and dried at 80 °C overnight.

Characterization

Thermogravimetric analyses (TGA) of approximately 1 mg of each compound is recorded on a TGA Q500 (TA Instruments) under either N_2 (N_2-TGA) or air (O_2-TGA), by equilibrating at 100 °C, and following a ramp of 10 °C min^{-1} up to 800 °C. Raman spectra are recorded with an Invia Renishaw microspectrometer (50) equipped with He–Ne laser at 532 nm. To avoid sample damage or laser-induced heating/crystallization of the materials, the incident power was kept at 1 % (full power of the laser is 100 mV). Powders are dispersed in EtOH, drop-cast onto a quartz slide and the solvent evaporated; at least 5 spectra per sample are recorded on different

Energy & Environmental Science Accepted Manuscript

Please do not adjust margins

View Article Online
DOI: 10.1039/C7EE03361C

areas of the sample in order to check the uniformity of the materials. Fourier Transform Infrared spectroscopy (FTIR) was measured in a System 2000 – Perkin Elmer spectrometer in an optical range of 370–4000 cm^{-1} at a resolution of 4 cm^{-1}. High resolution TEM (HRTEM) were acquired on a JEOL 2200FS microscope operating at 200 kV, equipped with an Energy Dispersive Spectrometer (EDX), in-column energy (Omega) filter, and high-angle annular dark-field (HAADF) detector.

Textural properties have been analyzed by N_2 physisorption at the liquid nitrogen temperature using a Micromeritics ASAP 2020 analyzer. Prior to the analysis, the sample was degassed at 120°C for 12h. The surface area has been calculated adopting the Brunauer-Emmett-Teller (BET) model while the pore size distribution has been assessed following the Barrett-Joyner-Halenda (BJH) Analysis.

Metal accessibility has been checked by CO chemisorption at 35°C using a Micromeritics ASAP 2020C analyzer. Prior to the analysis, the sample has been reduced in H_2 at 120°C for 1h and then degassed at the same temperature for 12h. CO chemisorption isotherm was recorded in the 1-400 mmHg range with an equilibration time of at least 5 minutes for each point. Reversible CO physisorption was subtracted by extrapolation to zero of the linear range of the isotherm. Metal surface area was calculated assuming a chemisorption stoichiometry CO:Pd = 1:1.

^{13}C-NMR were recorded on a 400 MHz Varian instrument. Samples were prepared by dissolving the electrolyte in D_2O and adding DMSO as internal standard.

Electrochemical measurements.

The electrochemical measurements were carried out at room temperature using an Autolab potentiostat/galvanostat (Model 302N) equipped with a three electrodes cell under a stream of purified gasses that depending on the experiments were pure N_2 or CO_2. The working electrode was a 3 mm glassy carbon electrode (GCE; CH Instrument, CH 104) which prior to its surface modification with the nanohorns' ink, was cleaned by polishing with 1.0 µm and 0.3 µm alumina slurries (micropolish Buehler) for 2 min and then washed with milliQ water. A platinum wire was used as counter electrode and an Ag/AgCl (3 M, NaCl) (CH Instrument, CH 111) as reference. All the reported potentials are converted to the RHE reference scale using E (vs. RHE) = E (vs. Ag/AgCl) + 0.210 V + 0.0591 V × pH when was necessary. Bulk electrolysis experiments for product analysis were carried out using modified Toray carbon paper (Alfa Aesar, TGP-H-60) as working electrode.

The nanohorns´ inks was prepared by dispersing 3 mg of prepared ox-SWCNHs, TiO_2/ox-SWCNHs or Pd@TiO_2/ox-SWCNHs powder in 1 mL of (1:0.09:0.02) water:EtOH:nafion (2.5 % in EtOH) solution. In each case the slurry was subjected to ultrasonic agitation for 90 min until a homogeneous dispersion was obtained. Finally, 20 µL of prepared ink was placed on the GCE surface and allowed to dry in an oven at 50 °C for 30 min. Catalytic electrodes obtained from diverse batch deposition and screened under identical conditions were found to display a performance variability of < 10 % in terms of current density, with analogous faraday efficiencies.

Cyclic voltammetry (CV) experiments were conducted in 0.1 M phosphate buffer solution, pH 7.4 at room temperature. Prior to each experiment, the electrolyte was saturated with N_2, Ar or CO_2 for 30 min. CV curves were recorded for the GCE coated with the ink layer in the potential range from 0.65 V to -0.85 V at scan rate of 0.05 V s^{-1}. Current densities are reported normalizing the current by the electroactive area determined by chronoamperometry.

Bulk electrolysis experiments for product analysis were carried out using Toray carbon paper as the working electrode modified with 200 microliters of 3.0 mg mL^{-1} dispersion (corresponding to a Pd loading of 38 µg cm^{-2}). The modification was done by drop casting and the current densities are reported normalized by the geometric area covered by the drop.

TOFs (H_2) calculation

The TOFs relative to production of H_2 were calculated using the following formula:

$$\text{TOF}(E) = \frac{Q(H_2) - Q(background)}{Q(Pd)\ X\ time} \text{ x FE}$$

Where TOF(E) are the TOF at an applied potential E, Q(H_2) is the total charge of the chronoamperometric experiment using the electrode with modified material, Q(background) is the background current measured in absence of Pd nanoparticles, Q(Pd) is the charge associated to electroactive Pd, and FE is the Faraday Efficiency.

Gas, ionic liquid chromatography and mass spectrometry

The products formed during the electrochemical reduction of CO_2 were analyzed by on-line gas chromatography (GC) and ionic chromatography (IC). For the gas phase analysis, the saturating gas (Ar or CO_2) was continuously bubbled through the electrolyte and analyzed on-line using an Agilent 7890 gaschromatograph equipped with a 10-way valve for injection and 2 analytical lines. CO possibly produced has been analyzed using a Permanent Gas/CO_2 column (parallel columns MolSieve 5A 10m x 0.32 mmID and PoraPlot Q 60m x 0.53mm ID) with He as carrier and connected to a methanizer and a FID detector. H_2 has been monitored using a MolSieve 5A (30m x 0.53 mm) column using Ar as carrier and connected to a TCD detector. The formate (HCO_2^-) formed in the liquid phase was quantified at the end of the electrolysis using a Metrohm 883 instrument equipped with a conductometric detector and a Metrosep A Supp5 250/4.0 column using a $NaHCO_3$ 1mM / Na_2CO_3 3.2 mM solution as mobile phase.

Published on 06 April 2018. Downloaded by Fudan University on 06/04/2018 19:06:53.
Energy & Environmental Science Accepted Manuscript

This journal is © The Royal Society of Chemistry 20xx

Please do not adjust margins

View Article Online
DOI: 10.1039/C7EE03361C

Published on 06 April 2018. Downloaded by Fudan University on 06/04/2018 19:06:53.

Qualitative analysis of formed HCOOH has been performed by SPME-GC/MS analysis. SPME extraction was performed with Supelco fibers coated with Carboxen/Polydimethylsiloxane (CAR/PDMS, thickness 75 µm). The method included inserting a new 1-cm CAR/PDMS fiber in a manual injection holder followed by preconditioning before the day's analyses. HCOOH was extracted by the static headspace method. During this step, the solution of $NaClO_4$ 0.5M after electrocatalytic reduction of CO_2 has been transferred into a 10 mL vial, sealed with a screw cap and heated at 50°C. Adsorption of HCOOH was performed exposing the fiber for 10 min in the headspace of the vial. The adsorbed molecules were desorbed by introducing the SPME fiber into the injector of a 7890 Ailent gaschromatograph. The injector, in splitless mode for 2 min, was set at 270°C. HCOOH was analysed using a DB-522ms column (J&W, 60 m × 0.32 mm ID, 20 µm film), using He as carrier gas. The mass spectra of the eluted HCOOH were acquired using a 5975C Agilent mass spectrometer, connected at the end of the GC column.

Faradaic Efficiency (FE) calculation

The formic acid FE was calculated by the formula

$$FE(HCOOH) = \frac{Q_{HCOOH}}{Q_{tot}} \; x\; 100$$

Q_{HCOOH} is the charge associated to formation of formic acid, calculated by the formula Q_{HCOOH} = nFe, where n is the number of moles of formic acid formed during a chronoamperometric experiment (measured by ionic chromatography), F is the Faraday constant, and e = 2, that is the number of electrons involved in the reduction of CO_2 to formic acid. Q_{tot} is the total charge passed in the chronoamperometric experiment, calculated by the formula

$$Q_{tot} = \int_0^t I(t)dt$$

(I = current, t = time of the experiment). For the calculation of FE(H_2) the method was the same but the charge was that associated to the formation of H_2 (Q_{H2}). The moles of H_2 are measured by gas chromatography.

Conclusions

Hybrid hetero structures have been synthesized by integrating small Pd NPs (1.5 nm) within a TiO_2 environment powered by highly conductive SWCNHs nano-scaffolds. The resulting nano-material provides a tunable platform for electrocatalytic H_2 storage/release technology, relying on CO_2 as a recyclable vector. In this perspective, the optimization of the interfacial synergy is of extreme interest as a function of the metal-hydride/metal-oxide "soft-hard" alternating phases and in combination with a tailored functionalization of the nano-carbon supports.

Conflicts of interest

There are no conflicts to declare.

Acknowledgements

The research leading to these results has received funding from the University of Trieste, INSTM, the Seventh Framework Programme [FP7/2007- 2013] under grant agreement n° 310651 (SACS project). MVB acknowledges the support of the "ICTP TRIL Programme, Trieste, Italy". C.T. acknowledges support from the Università degli Studi di Trieste, Finanziamento di Ateneo per progetti di ricerca scientifica, FRA2016.

Notes and references

1. M. Aresta, A. Dibenedetto and A. Angelini, *Chem. Rev.*, 2014, **114**, 1709-1742.
2. D. D. Zhu, J. L. Liu and S. Z. Qiao, *Adv. Mater.*, 2016, **28**, 3423-3452.
3. A. M. Appel, J. E. Bercaw, A. B. Bocarsly, H. Dobbek, D. L. DuBois, M. Dupuis, J. G. Ferry, E. Fujita, R. Hille, P. J. A. Kenis, C. A. Kerfeld, R. H. Morris, C. H. F. Peden, A. R. Portis, S. W. Ragsdale, T. B. Rauchfuss, J. N. H. Reek, L. C. Seefeldt, R. K. Thauer and G. L. Waldrop, *Chem. Rev.*, 2013, **113**, 6621-6658.
4. F. A. Armstrong and J. Hirst, *Proc. Natl. Acad. Sci. U. S. A.*, 2011, **108**, 14049-14054.
5. A. Bassegoda, C. Madden, D. W. Wakerley, E. Reisner and J. Hirst, *J. Am. Chem. Soc.*, 2014, **136**, 15473-15476.
6. J. A. Turner, *Science*, 2004, **305**, 972-974.
7. K. C. Christoforidis and P. Fornasiero, *ChemCatChem*, 2017, **9**, 1523-1544.
8. A. Álvarez, A. Bansode, A. Urakawa, A. V. Bavykina, T. A. Wezendonk, M. Makkee, J. Gascon and F. Kapteijn, *Chem. Rev.*, 2017, **117**, 9804-9838.
9. E. J. Popczun, C. G. Read, C. W. Roske, N. S. Lewis and R. E. Schaak, *Angew. Chem. Int. Ed.*, 2014, **53**, 5427-5430.
10. B. Cao, G. M. Veith, J. C. Neuefeind, R. R. Adzic and P. G. Khalifah, *J. Am. Chem. Soc.*, 2013, **135**, 19186-19192.
11. J. Kibsgaard, T. F. Jaramillo and F. Besenbacher, *Nat. Chem.*, 2014, **6**, 248-253.
12. Y. Li, H. Wang, L. Xie, Y. Liang, G. Hong and H. Dai, *J. Am. Chem. Soc.*, 2011, **133**, 7296-7299.
13. M. Tagliapietra, A. Squarcina, N. Hickey, R. De Zorzi, S. Geremia, A. Sartorel and M. Bonchio, *ChemSusChem*, 2017, **10**, 4430-4435.
14. J. Ying, G. Jiang, Z. Paul Cano, L. Han, X.-Y. Yang and Z. Chen, *Nano Energy*, 2017, **40**, 88-94.
15. R. Mazzaro, A. Boni, G. Valenti, M. Marcaccio, F. Paolucci, L. Ortolani, V. Morandi, P. Ceroni and G. Bergamini, *ChemistryOpen*, 2015, **4**, 268-273.
16. F.-Q. Shao, X.-Y. Zhu, A.-J. Wang, K.-M. Fang, J. Yuan and J.-J. Feng, *J. Colloid Interface Sci.*, 2017, **505**, 307-314.
17. B. C. Marepally, C. Ampelli, C. Genovese, T. Saboo, S. Perathoner, F. M. Wisser, L. Veyre, J. Canivet, E. A. Quadrelli and G. Centi, *ChemSusChem*, 2017, **10**, 4442-4446.
18. M. Ma, H. A. Hansen, M. Valenti, Z. Wang, A. Cao, M. Dong and W. A. Smith, *Nano Energy*, 2017, **42**, 51-57.
19. E. S. Gutterød, S. Øien-Ødegaard, K. Bossers, A.-E. Nieuwelink, M. Manzoli, L. Braglia, A. Lazzarini, E. Borfecchia, S. Ahmadigoltapeh, B. Bouchevreau, B. T. Lønstad-Bleken, R. Henry, C. Lamberti, S. Bordiga, B. M.

Energy & Environmental Science Accepted Manuscript

Please do not adjust margins

View Article Online
DOI: 10.1039/C7EE03361C

Weckhuysen, K. P. Lillerud and U. Olsbye, *Ind. Chem. Eng. Res.*, 2017, **56**, 13206-13218.

20. K. S. Egorova and V. P. Ananikov, *Angew. Chem. Int. Ed.*, 2016, **55**, 12150-12162.
21. X. Min and M. W. Kanan, *J. Am. Chem. Soc.*, 2015, **137**, 4701-4708.
22. C. J. Stalder, S. Chao and M. S. Wrighton, *J. Am. Chem. Soc.*, 1984, **106**, 3673-3675.
23. R. Kortlever, C. Balemans, Y. Kwon and M. T. M. Koper, *Catal. Today*, 2015, **244**, 58-62.
24. G. Valenti, A. Boni, M. Melchionna, M. Cargnello, L. Nasi, G. Bertoni, R. J. Gorte, M. Marcaccio, S. Rapino, M. Bonchio, P. Fornasiero, M. Prato and F. Paolucci, *Nat. Commun*, 2016, **7**, 13549.
25. S. Akbayrak, Y. Tonbul and S. Özkar, *Appl. Catal., B. Environ.*, 2017, **206**, 384-392.
26. A. Beltram, M. Melchionna, T. Montini, L. Nasi, P. Fornasiero and M. Prato, *Green Chem.*, 2017, **19**, 2379-2389.
27. M. Cargnello, J. J. D. Jaén, J. C. H. Garrido, K. Bakhmutsky, T. Montini, J. J. C. Gámez, R. J. Gorte and P. Fornasiero, *Science*, 2012, **337**, 713-717.
28. K. Bakhmutsky, N. L. Wieder, M. Cargnello, B. Galloway, P. Fornasiero and R. J. Gorte, *ChemSusChem*, 2012, **5**, 140-148.
29. M. Melchionna, A. Beltram, T. Montini, M. Monai, L. Nasi, P. Fornasiero and M. Prato, *Chem. Commun.*, 2016, **52**, 764-767.
30. L. Robert, H. Anming, P. John and Y. N. Zhou, *Nano-Micro Lett.*, 2013, **5**, 202-212.
31. J. Shen, B. Yan, M. Shi, H. Ma, N. Li and M. Ye, *J. Mater. Chem.* , 2011, **21**, 3415-3421.
32. G. Lu, H. Wang, Z. Y. Bian and X. Liu, *Sci World J*, 2013, Article ID 424617.
33. S. Berber, Y. K. Kwon and D. Tomanek, *Phys. Rev. B*, 2000, **62**, R2291-R2294.
34. G. Pagona, N. Tagmatarchis, J. Fan, M. Yudasaka and S. Iijima, *Chem. Mater.*, 2006, **18**, 3918-3920.
35. E. Bekyarova, K. Murata, M. Yudasaka, D. Kasuya, S. Iijima, H. Tanaka, H. Kahoh and K. Kaneko, *J. Phys. Chem. B*, 2003, **107**, 4681-4684.
36. K. Urita, S. Seki, S. Utsumi, D. Noguchi, H. Kanoh, H. Tanaka, Y. Hattori, Y. Ochiai, N. Aoki, M. Yudasaka, S. Iijima and K. Kaneko, *Nano Lett.*, 2006, **6**, 1325-1328.
37. M. Cargnello, N. L. Wieder, P. Canton, T. Montini, G. Giambastiani, A. Benedetti, R. J. Gorte and P. Fornasiero, *Chem. Mater.*, 2011, **23**, 3961-3969.
38. A. Hashimoto, H. Yorimitsu, K. Ajima, K. Suenaga, H. Isobe, A. Miyawaki, M. Yudasaka, S. Iijima and E. Nakamura, *P. Natl. Acad. Sci. USA*, 2004, **101**, 8527-8530.
39. V. Krungleviciute, C. A. Ziegler, S. R. Banjara, M. Yudasaka, S. Iijima and A. D. Migone, *Langmuir*, 2013, **29**, 9388-9397.
40. M. S. Dresselhaus, A. Jorio, M. Hofmann, G. Dresselhaus and R. Saito, *Nano Lett.*, 2010, **10**, 751-758.
41. O. Frank, M. Zukalova, B. Laskova, J. Kurti, J. Koltai and L. Kavan, *Phys. Chem. Chem. Phys.*, 2012, **14**, 14567-14572.
42. U. J. Kim, C. A. Furtado, X. M. Liu, G. G. Chen and P. C. Eklund, *J. Am. Chem. Soc.*, 2005, **127**, 15437-15445.
43. G. K. Ramesha, J. F. Brennecke and P. V. Kamat, *ACS Catal.*, 2014, **4**, 3249-3254.
44. M. Grden, M. Lukaszewski, G. Jerkiewicz and A. Czerwinski, *Electrochimica Acta*, 2008, **53**, 7583-7598.
45. K. Cheng, D. X. Cao, F. Yang, L. L. Zhang, Y. Xu and G. L. Wang, *J. Mater. Chem.*, 2012, **22**, 850-855.
46. Z. P. Li, X. C. Yang, N. Tsumori, Z. Liu, Y. Himeda, T. Autrey and Q. Xua, *ACS Catal.*, 2017, **7**, 2720-2724.
47. Q.-L. Zhu, N. Tsumori and Q. Xu, *J. Am. Chem. Soc.*, 2015, **137**, 11743-11748.
48. B. Niu, W. Xu, Z. D. Guo, N. Z. Zhou, Y. Liu, Z. J. Shi and Y. F. Lian, *J Nanosci Nanotechno*, 2012, **12**, 7376-7381.
49. I. Gerber, M. Oubenali, R. Bacsa, J. Durand, A. Goncalves, M. F. R. Pereira, F. Jolibois, L. Perrin, R. Poteau and P. Serp, *Chem-Eur J*, 2011, **17**, 11467-11477.
50. M. Cargnello, M. Grzelczak, B. Rodríguez-González, Z. Syrgiannis, K. Bakhmutsky, V. La Parola, L. M. Liz-Marzán, R. J. Gorte, M. Prato and P. Fornasiero, *J. Am. Chem. Soc.*, 2012, **134**, 11760-11766.

Published on 06 April 2018. Downloaded by Fudan University on 06/04/2018 19:06:53.

Energy & Environmental Science Accepted Manuscript

This journal is © The Royal Society of Chemistry 20xx

Please do not adjust margins

View Article Online
DOI: 10.1039/C7EE03361C

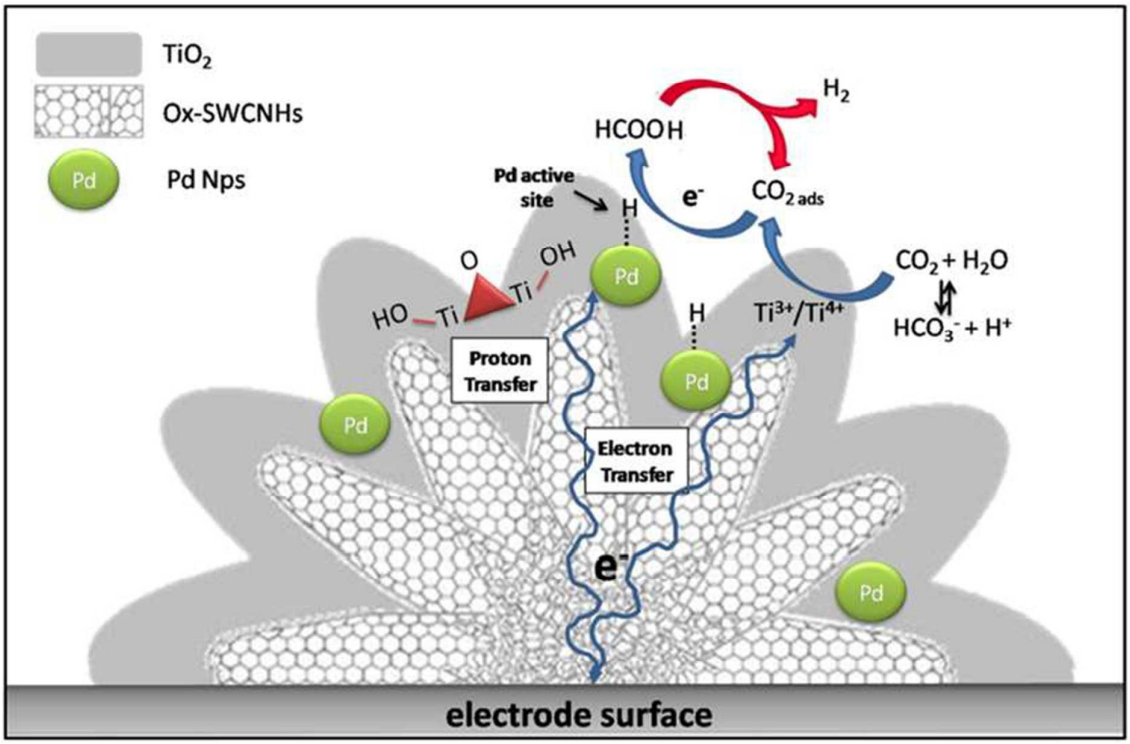

Published on 06 April 2018. Downloaded by Fudan University on 06/04/2018 19:06:53.

Energy & Environmental Science Accepted Manuscript

View Article Online
DOI: 10.1039/C7EE03361C

Published on 06 April 2018. Downloaded by Fudan University on 06/04/2018 19:06:53.

Broader Context

Sustainability is a central theme of today's scientific community. In conjunction with the growth of the world population and the fast depletion of fossil fuels, there is a need to define new concepts that diversify the supply of energy and make it sustainable. One intriguing solution is the environmentally benign (photo- or electro-assisted) reutilization of the anthropological CO_2: the strategy is to convert it back to carbon fuels, creating a carbon-neutral cyclic scheme. On the other hand, an alternative concept is the utilization of green energy vectors, such as hydrogen. However, reduction of CO_2 and H_2 evolution are both challenging processes, requiring a complex engineering of catalysts in order to trigger the reactions with low activation energy and high selectivity. Inspired by the natural Formate Dehydrogenase enzymes (FDH), herein we describe a nanostructured ternary electro-catalyst that is able to fulfil a double action: it can reduce CO_2 to formic acid with low overpotential and high current efficiency, and it can evolve hydrogen via sequential formic acid dehydrogenation. Mechanistic insights reveal that the nanocatalyst mimics the enzyme multi-functional behavior and the neat result is the use of CO_2 as a reversible energy vector.

Energy & Environmental Science Accepted Manuscript